Conference paper

Kateřina Horáková*, Stanislav Cichoň, Ján Lančok, Irena Kratochvílová, Ladislav Fekete, Petr Sajdl, Aneta Krausová, Jan Macák and Vladimír Cháb

Corrosion protection of zirconium surface based on Heusler alloy

DOI 10.1515/pac-2016-1030

Abstract: Fe and Si films were tested as corrosion protection layers for Zr in nuclear industry applications. Surface chemistry of Zr in dependence on the preparation conditions and layout of the films was complexly investigated by various spectroscopic and microscopic techniques. Corrosion experiments were carried out in autoclave conditions with in-situ Electrochemical Impedance Spectroscopy. A clean Zr surface is characteristic with disposition to disorder and rough morphology demonstrated in facets, steps or terraces. Upon deposition of Fe and Si atoms in amounts in the order of single monolayers and subsequent annealing at 400 °C, the original (1×1) Zr surface structure rearranges into $(2\sqrt{3}\times2\sqrt{3})R30°$. Corrosion experiments show that a thicker Si overlayer successfully suppresses oxygen uptake of the underlying Zr material by forming a diffusion barrier. The barrier effect of the films was also confirmed for hydrogen.

Keywords: electrochemistry; silicon; spectroscopy; SSC-2016; surface chemistry; water; zirconium.

Introduction

Zirconium is a very useful material for various technical applications. For many years, Zr alloys having low absorption cross-section of thermal neutrons have been used in the cores of water-cooled nuclear power reactors. Besides that, Zr is used as part of systems used for effective storage of hydrogen [1–4].

Zr alloy surface reacts with water steam in nuclear reactors. During this reaction Zr oxidizes and released hydrogen gas partly diffuses into the zirconium. The Zr alloys changed by oxygen/hydrogen diffusion are less dense and are mechanically weaker than the original material – their formation results in blistering and finally cracking. The processes of Zr alloys oxidation and hydrogenation lead to limitation criteria in justifying fuel rod life time. The design of a Zr cladding covered with a protecting layer calls for full knowledge of fundamentals of the Zr surface chemistry and structure, particularly the interaction with oxygen and hydrogen.

Several earlier studies investigated the surface chemistry of Zr with different techniques. Oxygen adsorption on Zr(0001) surface has been extensively studied using low energy electron diffraction (LEED), auger electron spectroscopy (AES) and work function measurement [5–11]. The most favorable oxygen adsorption

Article note: A collection of invited papers based on presentations at the 12th Conference on Solid State Chemistry (SSC-2016), Prague, Czech Republic, 18–23 September 2016.

***Corresponding author: Kateřina Horáková,** Institute of Physics, Academy of Sciences of the Czech Republic, Na Slovance 1999/2, 182 21 Prague 8, Czech Republic; and University of Chemistry and Technology Prague, Technická 5, 166 28 Prague 6, Czech Republic, Tel.: +420 266 052 565, E-mail: horakova@fzu.cz

Stanislav Cichoň, Ján Lančok, Irena Kratochvílová, Ladislav Fekete and Vladimír Cháb: Institute of Physics, Academy of Sciences of the Czech Republic, Na Slovance 1999/2, 182 21 Prague 8, Czech Republic

Petr Sajdl, Aneta Krausová and Jan Macák: University of Chemistry and Technology Prague, Technická 5, 166 28 Prague 6, Czech Republic

sites were found in the sub-surface region, similarly to the Ti (0001) surface. This interpretation is supported with studies of early stages of oxidation [12]. (2×2) LEED patterns of the O/Zr(0001) system were found at the oxygen coverage of 0.5 ML (monolayer). The structure is transformed to the (1×1) phase at coverage of 1 ML. For the (2×2) structure, there is a generally accepted model where the structure is composed of three (2×1) domains with oxygen atoms occupying the sub-surface octahedral sites located between the top and the second metal layer [6].

Theoretical ab initio simulations of Zhang et al. [13] dealt with the interaction of hydrogen with the Zr surface. Adsorption and dissociation of hydrogen were studied at the relaxed (0001) surface showing that the most stable equilibrium adsorption site can be ascribed to positions at the top-y channel, see [13]. However, potential energy surface calculations demonstrate nearly negligible energy barriers among adsorption states along the top-x and top-y channels. It has been found that the most stable chemisorbed state in the Zr(0001)/H system is realized through hybridization between the 1σ molecular orbital of H_2 and the 4d band edge of the Zr(0001) surface. The minimum energy path for the molecule dissociation was determined using the climb image nudged elastic band method, yielding the result that atomic hydrogen prefers to occupy the hcp site. The most stable and favorable are fcc-x channels where the dissociation process in H_2/Zr system is activated with the lowest energy barrier of 0.05 eV [13].

A protective layer has to work as an oxygen and hydrogen diffusion barrier in a wet environment. Recently, carbon was used in a very specific form for desired Zr alloys surface protection: the composite sp^3 and sp^2 phased polycrystalline diamond (PCD) layers created in microwave plasma enhanced linear antenna chemical vapor deposition apparatus [14]. Here, we present and examine an idea with a Fe–Zr–Si type Heusler alloy as a competitive corrosion protective film of a Zr cladding of nuclear fuel rods. More specifically, Fe_2ZrSi or FeZrSi Heusler alloys can be considered [15–17]. Initial investigations with the alloy were already performed by us in [18]. The first type of the protective film is Fe and Si deposited in-situ on a clean Zr surface up to coverage of one monolayer. A Si over layer about 60 nm in thickness deposited on a clean Zr surface represents the second type. This second type of samples was subjected to autoclave tests. The effect of Fe and Si on surface chemistry, morphology and corrosion behavior of Zr was examined and evaluated.

Experimental

We used NanoESCA (Oxford Instruments Omicron Nanoscience) instrument which is a photoemission spectrometer based on a photoelectron emission microscope (PEEM) column and a double hemispherical imaging energy filter [19]. The monochromatic Al $K\alpha_{1,2}$ X-ray source can be focused on the sample to illuminate a spot with a diameter between 10 and 100 μm. In the experiment, typically, the spot of 60 μm in diameter was used. The voltage of 15 kV is applied to accelerate the electrons emitted from the sample to enter the PEEM column. The overall resolution of the spectroscopic system working in the ESCA mode is 0.3–0.4 eV and 500 nm laterally. The design of the instrument offers switching between spatial and momentum imaging. We performed the k-space mapping employing HeI discharge lamp (FOCUS HIS 13). The energy resolution is 0.1 eV and the field of view ~ 4.5 μm in the real space. The equi-energy cuts through the k-space were done with a 0.1 eV step. The base pressure in the analytical chamber was better than 10^{-10} mbar. The quality and the crystal structure of the sample surface was analyzed and monitored with LEED in conjunction with the classical ESCA mode of the apparatus. Measured BEs are referenced to $E_F = 0$ eV. Identification of found peaks was carried out using XPS data banks [20, 21].

STM experiments were performed using a variable temperature scanning tunneling microscope (VT STM, Omicron GmbH) furnished with low energy electron diffraction (LEED) facility, sample transfer and ion sputtering. STM images were taken in the constant current mode. Tunneling currents varied in the range of 1–2 nA with the sample biases of 0.05–1.0 V. STM tips were typically fabricated from a cut-to-size piece of a high purity tungsten wire and sharpened by electrochemical etching. The pressure in the analytical chamber was around 10^{-10} mbar.

Zr(0001) single crystal was supplied by MaTecK (Material-Technologie & Kristalle GmbH). The sample was a disc of 10 mm diameter. The disc was actually composed of small crystallites with different crystallographic orientations. The (0001) face was found and identified using LEED measurements and k-space images. The cleaning procedure of the whole sample comprised of several cycles of Ar^+ sputtering and annealing up to 760 °C [12]. The quality of the surface was checked with XPS and LEED. Fe and Si were deposited on the sample clean surface sequentially either from a homemade evaporator (Si) or from a standard evaporator (Fe). The sample was held at RT (room temperature). Si was deposited in cycles to keep the pressure in the chamber $< 5 \times 10^{-9}$ mbar (direct heating with DC current, 10 times for 30 s). The surface coverage was estimated from the intensity of the Si 2p peak and occurrence of the $(2\sqrt{3} \times 2\sqrt{3})R30°$ structure. Fe was deposited from a rod using electron bombardment (FOCUS evaporator at pressure $< 8 \times 10^{-10}$ mbar).

Atomic force microscopy (AFM) measurements were carried out on a Bruker Dimension Icon AFM microscope using the PeakForce mode of measurement and using soft sharp ScanAsystAir tips (f = 70 kHz, k = 0.4 N/m) under ambient conditions. The AFM is used for measurement of insulators. We obtained AFM images of Zr oxides.

Alternatively, Fe coverage was achieved via Fe segregation from the Zr bulk upon annealing, circumventing any deposition. In fact, Zr is naturally contaminated with several elements that are only partially eliminated by purifying the metal [3]. In our sample, we found Fe, O, C, N and F to be the dominating contaminants in the dependence of the surface preparation (especially N and F). Segregation takes place in the temperature interval (300 °C, 700 °C). At higher temperatures, we observed Fe dissolution back into the bulk for both segregated and deposited Fe (see [22–24]).

Electrochemical Impedance Spectroscopy was employed to analyze the corrosion characterization of Zr with protective Si over layer. On 12 mm in diameter long disc of bare Zr (99 %), approximately 60 nm thick Si film was deposited by DC magnetron sputtering. The deposition was carried out in Ar plasma at 1 Pa with the Si target normal perpendicular to the sample surface. The base pressure in the chamber was 10^{-9} mbar. During 30 min long deposition, samples were heated up to 300 °C. The resulting film thickness was determined by profilometry and AFM. In-situ experiments were performed in high-pressure high-temperature loop (270 °C, 8 MPa) in aqueous solution of LiOH (2 mg · L^{-1} of Li^+ as LiOH). The working electrode was a disc of bare Zr and a disc of Zr coated by the Si film. The other details of in-situ experimental parameters are similar as in our previous work [25].

Results and discussion

XPS measurement

A typical survey spectrum of the clean Zr(0001)-(1 × 1) surface with identified peaks is shown in Fig. 1.

The Zr 3d spectra taken at the clean Zr(0001)-(1 × 1) surface are shown Fig. 2a. To the best of our knowledge, this is for the first time that two contributions have been distinguished. One of them (peak P at 179.1 eV BE) corresponds to the metallic state of Zr. The second one (peak Q) has a higher BE by about 0.2 eV. The Q peak reflects any minor structural or chemical changes of the surface. It is common for XPS measurements that the photoemission peak of a bulk origin preserves its parameters, unlike the surface one [21]. Thus, we consider the Q peak to the surface contribution either as bonds of Zr atoms with hydrogen or as a compensation of the relaxed surface. According to the theoretical prediction [6], the relaxation of the (1 × 1) Zr surface is insignificant, involving only top two atomic layers. It seems that the high number of steps and terraces observed in our AFM images might give rise to the Q peak. Earlier experiments demonstrated the presence of H at the surface or in the subsurface region at RT [12]. It is believed that hydrogen can be partially expelled from the sample bulk by cleaning in ultra high vacuum (UHV) [12, 27, 28]. Our impression following from the measurements is that the Q peak originates from the complex surface morphology and bonds with hydrogen are less probable.

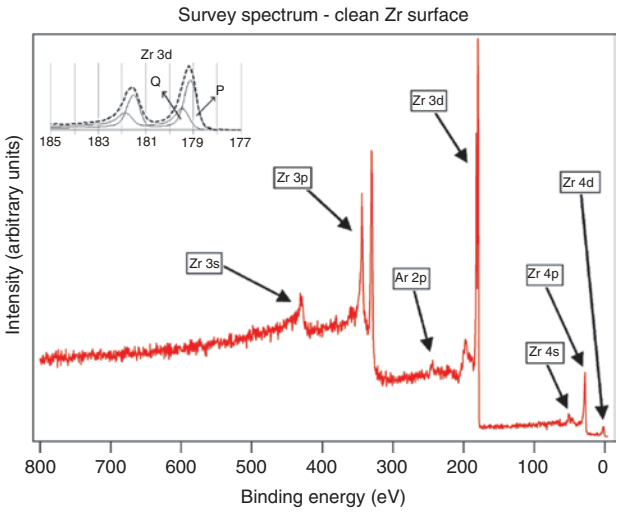

Fig. 1: Survey photoemission spectrum of clean Zr(0001)-(1×1) surface. The inset in the upper left corner shows Zr 3d core level.

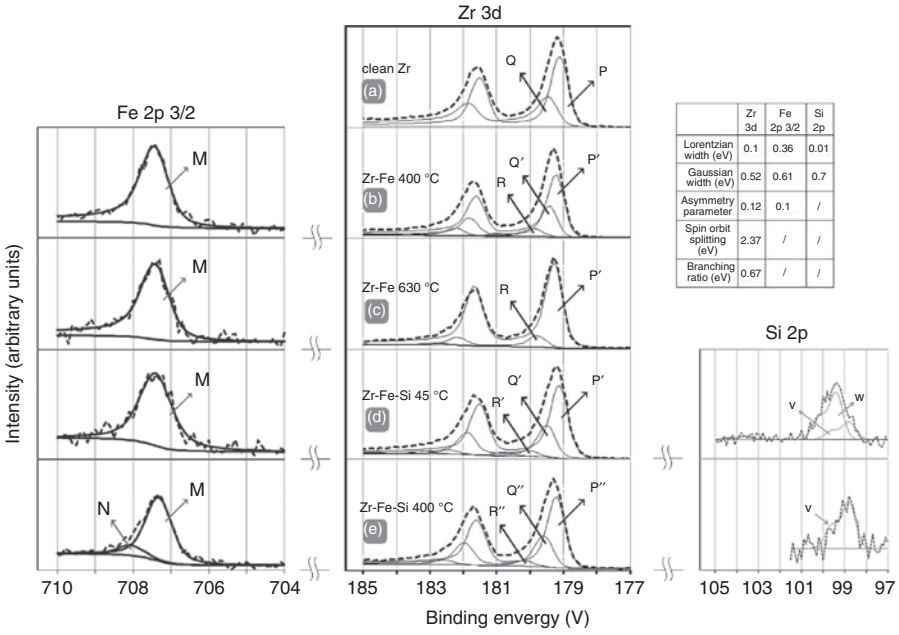

	Zr 3d	Fe 2p 3/2	Si 2p
Lorentzian width (eV)	0.1	0.36	0.01
Gaussian width (eV)	0.52	0.61	0.7
Asymmetry parameter	0.12	0.1	/
Spin orbit splitting (eV)	2.37	/	/
Branching ratio (eV)	0.67	/	/

Fig. 2: Core level photoemission spectra of Zr(0001) surfaces with or without Fe and Si. (a) clean Zr(0001)-(1×1) at room temperature, (b) Zr with deposited Fe and annealed at 400 °C, (c) Zr with deposited Fe and annealed at 630 °C, (d) Zr with deposited Fe and Si at 45 °C, (e) Zr with deposited Fe and Si and annealed at 400 °C. Doniach-Šunjić line profiles were used for fitting [26].

Zr surface covered by Fe possesses amorphous structure with no LEED spots. Its chemical state is obvious from the photoelectron spectra of Zr 3d and Fe 2p in Fig. 2b and c. Zr 3d spectrum as a whole is shifted about 0.1 eV to lower BE. After annealing at 400 °C, Q peak is split in two parts. The first part dominates at lower BE 179.2 eV (Q′) and the second part forms a new peak R at 179.8 eV BE. R peak intensity increases moderately with the annealing temperature up to 650 °C, whereas it starts to decrease slowly above 700 °C, signaling Fe dissolution. The surface becomes saturated with Fe close to the annealing temperature 630 °C. Fe deposition is accompanied with reduction of the Q′ peak intensity to zero value (see Fig. 2c). The nature of the surface remains amorphous irrespective of the annealing temperature as no LEED diffraction spots were

detected. The Fe 2p spectrum (Fig. 2b) displays a single peak at 707.4 eV BE for the segregated surface and the evaporated layer, as well. The value moderately differs from the one measured at a bulk sample.

Si was deposited on the Zr–Fe surface at 45 °C (see Fig. 2d). The structure of the new surface retains the amorphous character. The Zr 3d spectrum is composed of three peaks (P′, Q′ and R′). The BE values of the peak P′ and Q′ are identical with pure Zr–Fe surface, except the R peak having been shifted to higher BE. The full width half maximum (FWHM) value of the Fe 2p slightly increases, signaling an increased disorder at the surface. The Si 2p spectrum exhibits an envelope corresponding to two chemical states. The first state at 99.3 eV BE represents Si atoms and the second one at 98.75 eV BE Si signalizes a bonding with one of the elements or a different adsorption site at the surface [29, 30]. Annealing at T ≥ 400 °C yields a single peak in the Si 2p spectrum at 98.8 eV BE, which implies just one type of bonding of Si Fig. 2e. After treatment at temperatures ≥ 400 °C, the R′ (R″) peak of the Zr 3d spectrum shifts approximately by 0.5 eV to higher BE (180.3 eV). We ascribe it to the formation of Zr silicides at these temperatures [29–31]. The N structure in the Fe 2p spectrum evidences a more complex chemical nature of the bonding, like for example Zr–Fe–Si.

Topography measurement

The clean Zr(0001) surface shows characteristic (1×1) diffraction spots (Fig. 3a) in the full range of the electron beam voltage between 15 and 150 V. The images display relatively low background and not very sharp diffraction. The Zr–Fe surface with deposited Si shows a diffraction pattern which we identified to be (2√3×2√3)R30° reconstruction using the software for LEED images analysis [32]. The image consists of external six spots

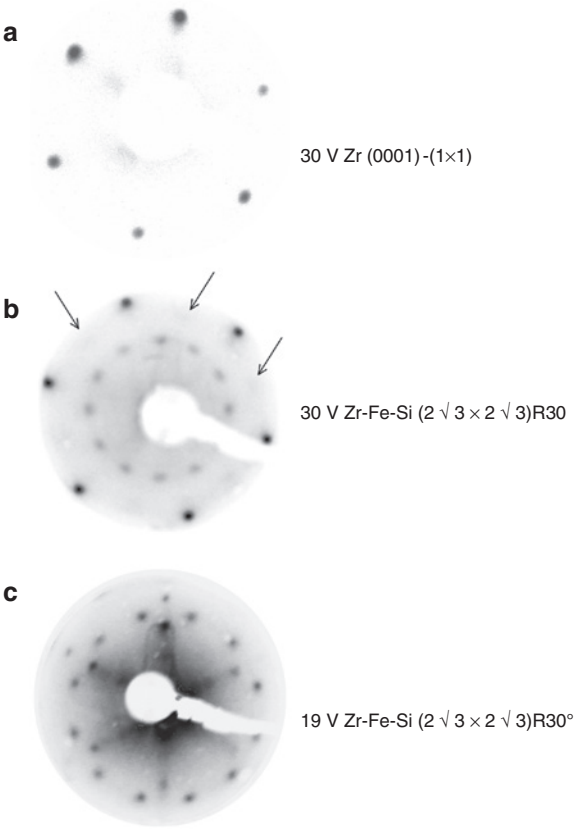

Fig. 3: LEED patterns. (a) (1×1) pattern of Zr(0001) crystal, (b) and (c) diffraction spots with trigonal symmetry inside basic (1×1) pattern of Zr–Fe–Si. Arrows in panel (b) point to residual very weak (1×1) pattern of Zr(0001) substrate. Panel (c) is structure measured with beam energy 19 V and in panel (b) there is the same structure but with higher beam energy 30 V. For more details about the patterns, see [18].

rotated 30° towards the (1×1) patterns of the clean Zr(0001) and 12 internal spots that are seen at the beam energy between 19 and 39 V. At the beam energy around 30 eV, faint Zr(1×1) spots are observable (see arrows marking spots as a guide to the eye in the image Fig. 3b). Annealing above ~600 °C smears the $(2\sqrt{3}\times 2\sqrt{3})$ R30° patterns. Although most of Si is bonded in the new structure, there is still relatively high degree of disorder at the surface.

AFM images taken on the single crystal surface display a hilly surface that is split in a number of small terraces, see Fig. 4. The images were acquired in the ambient atmosphere that causes high degree of the oxidation represented with white spots. The corrugation, in terms of Root Mean Square Roughness (R_{RMS}), is 6.9 nm for the area of 20 μm×20 μm and reaches 11.7 nm for the area of 90 μm×90 μm. It can be reduced with increasing the annealing temperature. Nevertheless, this procedure is restricted due to irreversible phase transition between hcp and bcc structures at 862 °C [3] and a contaminant segregation or dissolution in the bulk. Similarly to AFM images, also STM images (Fig. 4) show the surface with many morphological features such as terraces, facets and steps. The size of terraces and facets observed at the surface are relatively small (~100 nm) in the comparison with other metal surfaces. This type of the disorder is characterized with high density of steps, vacancies, edges, etc. Atoms forming these features have certainly different BE reflected in the peak Q of the Zr 3d spectrum (Fig. 2). In Fig. 5 we can see Zr(0001) surface with a higher degree of oxidation as white islands decorating steps or borders of terraces. It is an evidence of their higher reactivity.

In Fig. 6 is shown the AFM image of the Zr polycrystalline surface. The images were taken on a single crystallite. The left panel exhibits a high degree of the oxidation during the transport from the UHV conditions. The facets are covered with different number of oxide layers that copy the Zr substrate. The right panel shows the surface covered with Si. It protects the surface from the reaction with O. The white chains demonstrate an initial degree of oxidation during the Si deposition [33]. In Fig. 7, the 60 nm Si layer on the poly Zr displays worm like structure that is presumably not ideal for a surface protection.

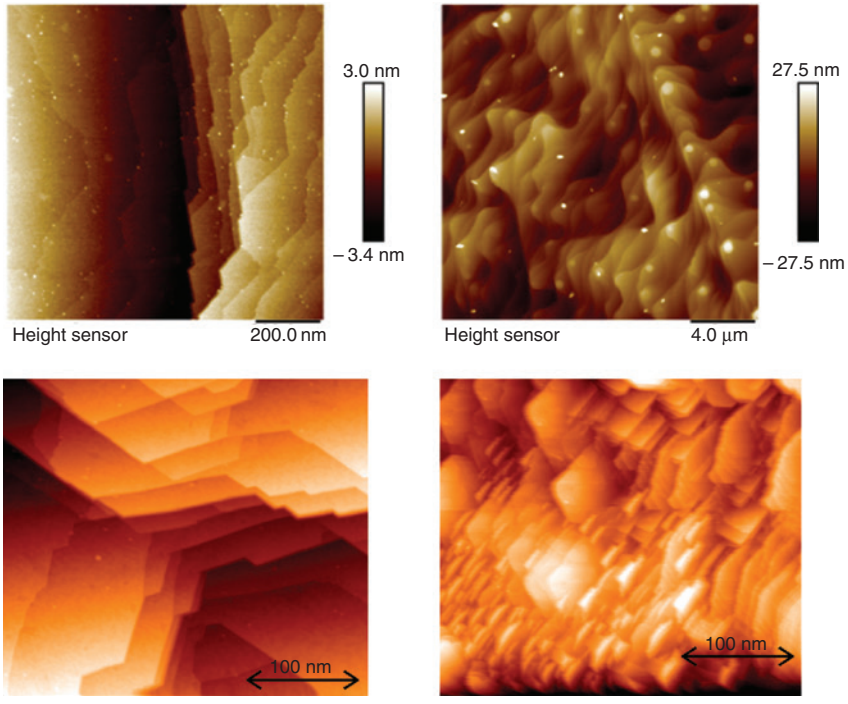

Fig. 4: AFM and STM images of clean Zr(0001) surface. AFM: Left image – 1 μm×1 μm area. Right image – 20 μm×20 μm area. The images represent different parts of the surface more (left) or less ordered (right). Both show very high density of terraces, steps or other types of defects. STM: Left image demonstrates a typical size of the terraces at the clean surface arranged in valleys and blocks. Right image displays a strong tendency towards faceting of the surface. Similarly to AFM, high density of defects is recognized on this surface. The defects cause the presence of P and Q peaks in the Zr 3d photoelectron spectrum (Fig. 2).

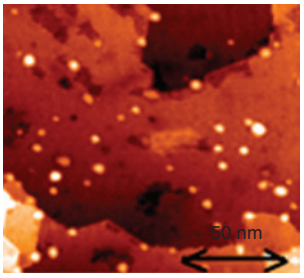

Fig. 5: STM image of oxidized Zr(0001)-(1×1) surface. The surface is covered with different structures that represent altering content of oxygen. The highest degree of oxidation is represented with small bright protrusions originating from the formation of ZrO_2 islands. They are attached mostly to surface defects.

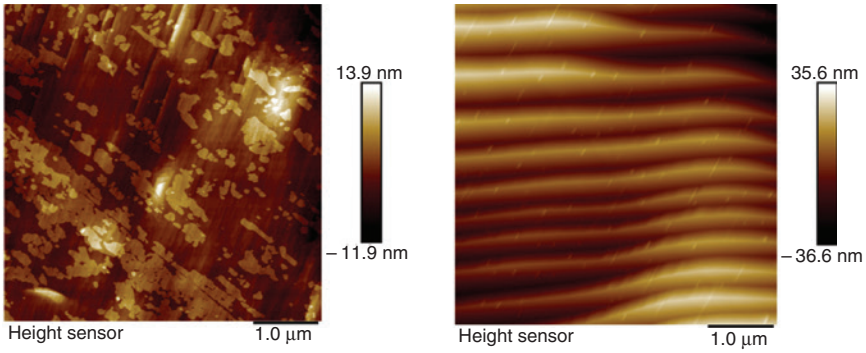

Fig. 6: AFM images of polycrystalline Zr surfaces. The selected crystallite shows a strong tendency of faceting on the submicron scale. Left panel – oxidized surface covered with irregular islands arranged in multilayer film. Right panel – facets of polycrystalline Zr surface covered with homogenous film of Si (2–3 monolayers). Short white chains seen in the image (right panel) originated during the Si deposition due to the evaporator degassing and they reflect surface interaction with oxygen.

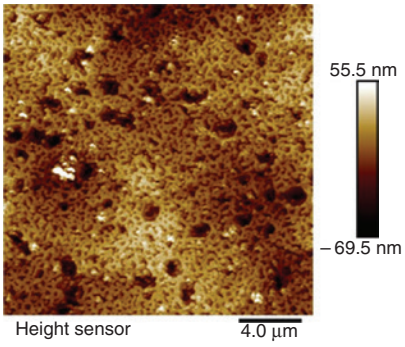

Fig. 7: AFM image of polycrystalline Zr surface covered with ~60 nm Si film as protective layer. Black spots seen on the surface are depressions in the layer. Such samples were submitted to autoclave tests (see Fig. 9).

k-space mapping

The Zr DOS of the valence band is formed of hybridized spd electrons [34, 35]. The valence band spectrum of previous experimental work [12] was done with angle resolved measurement at SR source. The Fermi edge is dominated with Zr d electrons and at – 1.2 eV BE peak was prescribed to the H induced feature. The identification of this structure was done on the base of the temperature behavior: The peak is gradually erased with increasing temperature and a subsequent cooling annuls it.

We mapped the dispersion function E vs k with equi-energy cuts through the band structure providing images with acceptable momentum and energy resolutions [36]. The left panel of Fig. 8 displays selected images of local densities of electronic states (LDOS) at E_F and at – 1.2 eV BE in the first BZ. At the clean Zr, the central part around the Γ point dominates the k-space E_F cut. The central hexagonal part is surrounded with six LDOS of trigonal symmetry as the entire cut corresponding to the (0001) face is. The k-space images match well the theoretical calculations of the electron structure presented in [34]. The mapping was done for the energy span between E_F and the bottom of the valence bands. The cuts show a high LDOS well localized in the center of BZ for the energies between – 0.7 eV and – 1.3 eV in the agreement with the previous interpretation [12] that the observed peak in LDOS results from the H–Zr interaction. Regarding the Zr–Fe–Si $(2\sqrt{3}\times 2\sqrt{3})R30°$ surface, it shows significant changes in electronic structure when compared with the clean Zr (see left panel of the Fig. 8). The cut close to E_F possesses 30° rotated symmetry with substantially lower LDOS at Γ point and flower like patterns. The Si bonding at the Zr–Fe–Si surface is fully reflected in LDOS structure forming the – 1.2 eV cut. The flower like features of this cut are preserved. However, the central H induced peak is replaced with six well-separated local maxima. Thus, we believe that the $(2\sqrt{3}\times 2\sqrt{3})R30°$ structure at the Zr–Fe–Si surface is a consequence of H being depleted in the sample topmost surface layers or H possibly substituted with Si forming Zr–Si bond.

Electrochemical impedance spectroscopy

Impedance spectra of Si-coated and uncoated samples are given in Fig. 9. The experimental data were approximated by transfer function of the following form:

$$Z(\omega) = R_e + \left[R_{ox}^{-1} + C_{ox} j\omega + Q_{ox} (j\omega)^{-\alpha} \right]^{-1} + ([R_{ct} + Y_0^{-1} (j\omega)^{-0.5} \tanh\{B(j\omega)^{-0.5}\}]^{-1} + Q_{dl} (j\omega)^{-\beta})^{-1} \quad (1)$$

Here, R_e represents the electrolyte resistance. The second term represents complex capacitive (C_{ox}, Q_{ox}) and resistive (R_{ox}) response of oxide or oxide and remnants of the Si film, j stands for imaginary unit and ω for angular frequency. The third term represents mass transfer (parameters Y_o and B) and charge transfer (Y_o, B, R_{ct} and Q_{dl}) across the oxide or oxide-Si layer. Exponents α and β express a degree of deviation of the parameters Q_{ox} and Q_{dl}, respectively from ideal capacitive behavior.

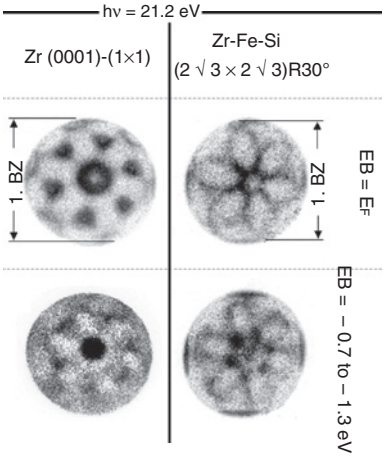

Fig. 8: PEEM images (k-space). Top left: Zr(0001) crystal at the Fermi edge. Top right: Zr–Fe–Si at the Fermi edge. Bottom left: slice of Zr(0001) crystal representative of the energy interval spanning from – 0.7 to – 1.3 eV under the Fermi edge. Bottom right: slice of Zr–Fe–Si representative of the energy interval spanning from – 0.7 to – 1.3 eV under the Fermi edge. For more details about the images, see [18].

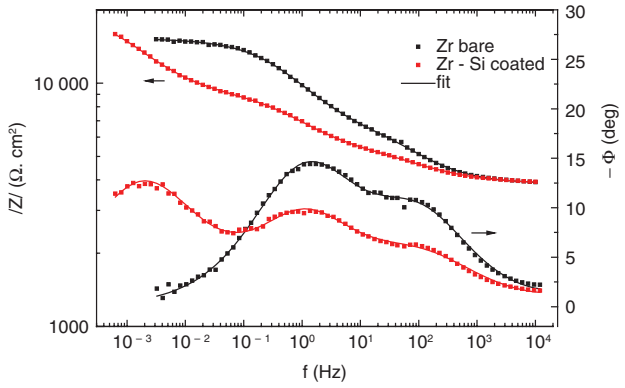

Fig. 9: Bode plots of impedance spectra of bare (clean) Zr and Si coated Zr. Measured in autoclave after exposure for 700 h in diluted LiOH at 270 °C and 8 MPa.

Table 1: Corrosion-related parameters estimated by fitting of the data by function (1).

	C_{ox} F · cm^{-2}	B s$^{-0.5}$	Y_o Ω^{-1} · s$^{0.5}$ · cm^2	R_{ct} Ω · cm^2
Uncoated	0.98e-6	0.79	0.00084	8300
Si-coated	2.3e-6	15.75	0.00308	4470

Both bare Zr/oxide and Zr/oxide/Si film impedance dispersion are characteristic with two time constants in frequency range of 10^{-1}–10^4 Hz. Main difference between the two cases appears in the frequencies below 10^{-1} Hz. In case of the un-coated sample, the shape of low frequency end of impedance dispersion is purely resistive, while in case of Si-coated sample new time constant appears. This part of spectra enables estimation of mass and charge transfer parameters (B and Y_o parameters in the above given function) connected with diffusion of charged species (in this case oxygen anions) across the surface layers. In case of uncoated sample, the diffusion time constant is moved to higher frequencies (approximately between 0.1 Hz and 20 Hz) and is effectively merged with a time constant formed by charge transfer resistance (R_{ct}) and Helmholtz layer dispersive capacitance at the oxide-electrolyte interface (Q_{dl}). The B/Y_o ratio, which has the meaning of diffusion resistance gives in the case of coated sample values around 5000–6000 Ω · cm^2, while for un-coated samples values around 1000–2000 Ω · cm^2 were found (Table 1). It means that under conditions of the experiment 2–3 times lower diffusion rate is typical for coated sample compared to the un-coated one. It corresponds to more than 2 times lower value of capacitance C_{ox} and, consequently, a thicker oxide, formed due to corrosion in hot LiOH solution on the un-coated sample. The Si layer and its remnants form thus an effective diffusion barrier and suppress the corrosion rate of Zr in high temperature Li+ containing water.

Conclusions

LEED analysis, STM images and AFM images of the clean Zr(0001) surface reveal a relatively high degree of disorder stabilized with high density of steps and small terraces. The rough surface can be healed with annealing close to the Zr phase transition. In terms of electronic structure, the clean Zr(0001)-(1×1) surface exhibits a good agreement with calculations. The evidence of H at surface or subsurface regions was found around – 1 eV below E_F. After Fe deposition, the resulting surface structure is amorphous. Addition of Si by deposition on the Zr–Fe amorphous layer has a very strong effect on the ordering of the surface. Slight annealing at 400 °C of the Zr–Fe–Si system produces a new structure with (2√3×2√3)R30° symmetry. Electronic

structure of the $(2\sqrt{3}\times 2\sqrt{3})R30°$ surface demonstrates presence of different symmetry in comparison with the clean Zr(0001) surface. More specifically, LDOS cuts around −1 eV below E_F demonstrate vanishing of the undesirable H induced feature upon the Zr–Fe–Si alloy $(2\sqrt{3}\times 2\sqrt{3})R30°$ surface formation. Thus, using Fe and Si atoms, the Zr(0001) surface can be transformed into a stable Heusler-like alloy which addresses the problem with hydrogen uptake by the Zr cladding.

Autoclave corrosion tests demonstrate good protection capabilities of the Si overlayer. 2–3 times lower diffusion rate was typical for Si coated Zr sample compared to the un-coated one. The Si layer and its remnants form an effective diffusion barrier and suppress the corrosion rate of Zr in high temperature Li+ containing water.

As can be seen, combination of different materials for Zr alloy anticorrosion protection (polycrystalline diamond plus Heusler alloys) seems to be very promising.

Acknowledgments: The authors acknowledge financial support from the Czech Science Foundation, Grant No. 16-03085S, 15-05095S, and from the Ministry of Education, Youth and Sports of the Czech Republic Grant No. LM2016088 and LO1409. S. C. acknowledges financial support from the Czech Science Foundation, Grant No. 17-19910Y.

References

[1] Ch. Hellwig. "Core Components in LWRs", EPFL Doctoral Course EY-F02: Materials for Nuclear Fission Reactors, Paul Scherrer Institut, Villigen, Switzerland, Autumn Semester, 2007.
[2] Y. Chen, M. Urquidi-Macdonald, D. D. Macdonald. *J. Nucl. Mater.* **348**, 133 (2006).
[3] R. H. Nielsen, G. Wilfing. *Zirconium and Zirconium Compounds. Ullmann's Encyclopedia of Industrial Chemistry*. Wiley-VCH Verlag GmbH & Co. KGaA (2010).
[4] M. Große, E. Lehmann, M. Steinbrück, G. Kühne, J. Stuckert. *J. Nucl. Mater.* **385**, 339 (2009).
[5] P. C. Wong, K. C. Hui, B. K. Zhong, K. A. R. Mitchell. *Solid State Commun.* **62**, 293 (1987).
[6] C.-S. Zhang, B. J. Flinn, I. V. Mitchell, P. R. Norton. *Surf. Sci.* **245**, 373 (1991).
[7] Y. M. Wang, Y. S. Li, K. A. R. Mitchell. *Surf. Sci.* **342**, 272 (1995).
[8] Y. M. Wang, Y. S. Li, K. A. R. Mitchell. *Surf. Sci Lett.* **343**, L1167 (1995).
[9] Y. M. Wang, Y. S. Li, K. A. R. Mitchell. *Surf. Sci.* **380**, 540 (1997).
[10] C.-S. Zhang, B. J. Flinn, P. R. Norton. *Surf. Sci.* **264**, 1 (1992).
[11] B. Li, A. R. Allnatt, C.-S. Zhang, P. R. Norton. *Surf. Sci.* **330**, 276 (1995).
[12] V. Dudr, F. Šutara, T. Skála, M. Vondráček, N. Tsud, V. Matolín, K. C. Prince, V. Cháb. *Surf. Sci.* **600**, 3581 (2006).
[13] P. Zhang, S.-X. Wang, J. Zhao, C.-H. He, P. Zhang. *J. Nucl. Mater.* **418**, 159 (2011).
[14] P. Ashcheulov, R. Škoda, J. Škarohlíd, A. Taylor, L. Fekete, F. Fendrych, R. Vega, L. Shao, L. Kalvoda, S. Vratislav, V. Cháb, K. Horáková, K. Kůsová, L. Klimša, J. Kopeček, P. Sajdl, J. Macák, S. Johnson, I. Kratochvílová. *Appl. Surf. Sci.* **359**, 621 (2015).
[15] D. I. Bilc, G. Hautier, D. Waroquiers, G.-M. Rignanese, P. Ghosez. arXiv:1405.4685v2 [cond-mat.mtrl-sci].
[16] D. I. Bilc, G. Hautier, D. Waroquiers, G.-M. Rignanese, P. Ghosez. *Phys. Rev. Lett.* **114**, 136601 (2015).
[17] Y. Du, W. Xiong, W. Zhang, H. Chen, W. Sun and MSIT® (2008), G. Effenberg (Ed.), MSI Eureka in SpringerMaterials, Fe-Si-Zr Ternary Phase Diagram Evaluation, http://materials.springer.com/msi/docs/sm_msi_r_10_010066_01, 10.10066.1.6 (MSI Materials Science International Services GmbH, Stuttgart © 2014).
[18] K. Horáková, S. Cichoň, J. Lančok, P. Sajdl, V. Cháb. *Surf. Sci.* **657**, 28 (2017).
[19] *NanoESCA Operating Manual PEEM Mode*, 1st ed.; Omicron Nanotechnology: Taunusstein, Germany (2006).
[20] J. F. Moulder, W. F. Stickle, P. E. Sobol, K. D. Bomben. *Handbook of X-ray Photoelectron Spectroscopy*, Physical Electronics, USA (1992).
[21] J. F. Watts, J. Wolstenholme. *An Introduction to Surface Analysis by XPS and AES*, John Wiley & Sons Ltd, England (2003).
[22] J. R. Chelikowsky. *Surf. Sci.* **139**, L197 (1984).
[23] P. M. Ossi. *Surf. Sci.* **201**, L519 (1988).
[24] A. V. Ruban, H. L. Skriver, J. K. Nørskov. *Phys. Rev. B* **59**, 15990 (1999).
[25] A. Krausová, J. Macák, P. Sajdl, R. Novotný, V. Renčiuková, V. Vrtílková. *J. Nucl. Mater.* **467**, 302 (2015).
[26] S. Doniach, M. Sunjic. *J. Phys. C Solid State* **3**, 285 (1970).
[27] J. Park, W. Kim, M. Won. *Mater. Trans.* **48**, 1012 (2007).
[28] K. A. Terrani, M. Balooch, D. Wongsawaeng, S. Jaiyen, D. R. Olander. *J. Nucl. Mater.* **397**, 61 (2010).

[29] W. Liu, J. Liang, X. Zhou, X. Long. *Mater. Lett.* **122**, 220 (2014).
[30] H. Yanagisawa, K. Sasaki, H. Miyake. Y. Abe, *Jap. J. Appl. Phys.* **39**, 4110 (2000).
[31] P. Villars. Material Phases Data System (MPDS), CH-6354 Vitznau, Switzerland (Ed.), SpringerMaterials, Si-Zr Binary Phase Diagram 0-100 at. % Zr, http://materials.springer.com/isp/phase-diagram/docs/c_0102160, c_0102160 (Springer-Verlag GmbH, Heidelberg, © 2014).
[32] LEEDpat, Version 4.2, utility by K.E. Hermann (FHI) and M.A. Van Hove (HKBU), Berlin/Hong Kong, 2014; see also http://www.fhi-berlin.mpg.de/KHsoftware/LEEDpat/index.html.
[33] N. Stojilovic, E.T. Bender, R.D. Ramsier. *Prog. Surf. Sci.* **78**, 101 (2005).
[34] Fermi Surface Explorer, © C. Lehmann, S. Sinning, P. Zahn, H. Wonn, I. Mertig, Dresden 1996–1998.
[35] M. Kurahashi, Y. Yamauchi. *Surf. Sci.* **420**, 259 (1999).
[36] Y. Polyak, V. Drchal, J. Kudrnovský, O. Heczko, J. Honolka, V. Cháb, J. Lančok. *Phys. Rev. B* **91**, 165115 (2014).